Flux Control Modulation for the Dual Active Bridge DC/DC Converter

Niklas Fritz[*], *Mohamed Rashed*[*], *Serhiy Bozhko*[*], *Fabrizio Cuomo*[†] *and Pat Wheeler*[*]

[*] *The Department of Electrical and Electronic Engineering, The University of Nottingham, United Kingdom*

[†] *Leonardo Aircraft Division, Naples, Italy*

niklas.fritz@rwth-aachen.de

Keywords: Dual Active Bridge, Modulation, Flux linkage, Switching losses, More Electric Aircraft

Abstract

This paper introduces a novel modulation technique for the single phase Dual Active Bridge (DAB) in which the switching frequency and transformer flux are modulated to achieve improved power transfer characteristics and reduced converter losses. By analyzing the DAB, it is noticed that in the traditional Single Phase Shift (SPS) modulation, the transformer flux linkage decreases with increasing power. The proposed Flux Control Modulation (FCM) counteracts this decrease and aims to keep the transformer utilization constant on the whole load range by a reduction in switching frequency. This has two effects: First, the reduced frequency substantially lowers switching losses and second, the power transfer characteristic of the DAB is linearized, facilitating the control of this converter. The new modulation technique is validated by simulation.

1 Introduction

Power Electronics is a key enabling technology in the development of next-generation aircraft systems. The More Electric Aircraft (MEA) is a concept aiming to replace traditional hydraulic, pneumatic, mechanical, and other systems with more efficient, lightweight and reliable electrical systems, cutting down fuel consumption and operating cost [1, 2]. However, this trend pushes the aircraft Electrical Power System (EPS) to the multi-megawatt range. The ASPIRE project deals with the development of an EPS for future aircraft, which can tackle the challenges that the MEA concept introduces. A high power density 3 kW single phase Dual Active Bridge (DAB) is developed for the implementation of a 'smart grid' concept in future EPS.

When analyzing the traditional Single Phase Shift (SPS) modulation for the DAB, it becomes clear that the peak flux linkage of the transformer decreases with increasing power transfer. This implies that the transformer has to be designed for no load, and that it is not fully utilized during power transfer.

In general, improvement of modulation strategies for the DAB has been subject to research work [3–9]. Qualitatively, variable frequency modulation has been reported in literature as a means of efficiency improvement [10–14]. However, the modulation strategy presented in this paper will provide the mathematical background for optimization of the frequency adaptation.

Based on thorough analytical modeling of the DAB, this paper introduces an improved modulation technique called Flux Control Modulation (FCM), which is derived from SPS modulation. By variation of the switching frequency, FCM aims to keep the utilization of the transformer core constant on the whole load range. This not only improves the overall operating efficiency of the DAB, but also linearizes the power transfer characteristic of the DAB and hence simplifies the control design of the converter.

Section 2 gives a brief overview of the DAB. Section 3 introduces an analytical model of SPS modulation. Based on the outcomes of this analysis, FCM is introduced in section 4. A detailed comparison of SPS modulation and FCM is presented in section 5, followed by validation in section 6.

2 The Single Phase Dual Active Bridge

The DAB was first proposed in 1991 [15]. The generic single phase variant of the DAB is depicted in Fig. 1.

The single phase DAB consists of two active H-Bridges equipped with switching devices such as MOSFETs or IGBTs, and a high frequency transformer providing galvanic isolation and leakage inductance. V_P denotes the primary side DC voltage and V_S denotes the secondary side DC voltage. The original modulation strategy for this topology is called Single Phase Shift modulation (SPS), which is depicted in Fig. 2 [15]. Both H-Bridges operate at 50 % duty cycle, but phase shifted in time by the angle ϕ. The output voltages of the primary and secondary side H-Bridge are denoted $v_\mathrm{P}(t)$ and $v_\mathrm{S}(t)$, respectively. Using the transformer turns ratio n, all secondary side quantities are referred to the primary side, which is indicated by a dash. The waveforms $v_\mathrm{P}(t)$ and $v_\mathrm{S}^{'}(t)$ are shown in Fig. 2a. The voltage difference $v_\mathrm{P}(t) - v_\mathrm{S}^{'}(t)$ across the leakage inductance L of the transformer will result in a quasi-square waveform of high

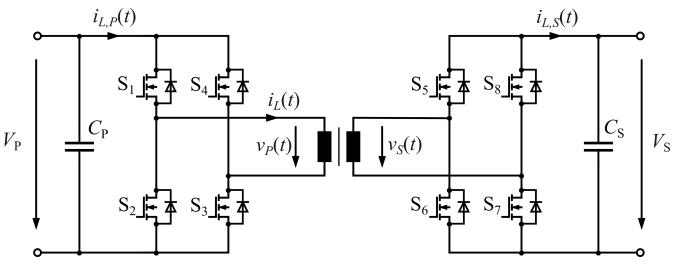

Figure 1: The Dual Active Bridge topology, single phase.

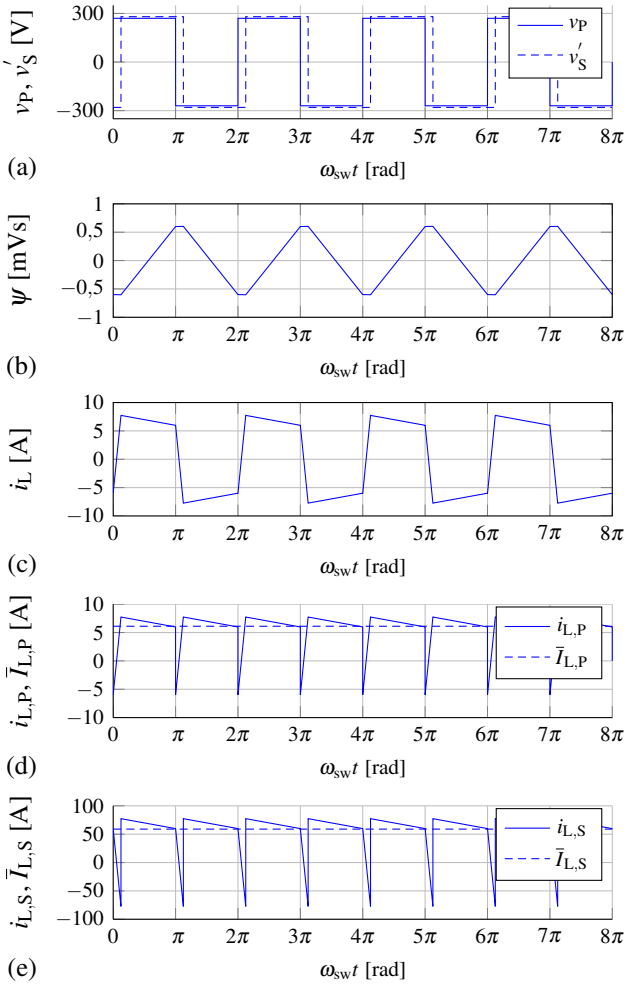

Figure 2: The generic Single Phase Shift (SPS) modulation. (a) Output voltages of the H-Bridges. (b) Transformer flux linkage. (c) AC link current. (d) Primary side rectified current and primary side DC current. (e) Secondary side rectified current and secondary side DC current.

frequency AC current in the transformer, $i_L(t)$ (see Fig. 2c). As shown in Fig. 1, the input currents of the primary and secondary side H-Bridge are denoted $i_{L,P}(t)$ and $i'_{L,S}(t)$, respectively. They are plotted in Fig. 2d and Fig. 2e, respectively. The current ripple is filtered by the primary and secondary side DC capacitors C_P and C_S. The average currents provided by the primary and secondary side DC buses are denoted $\bar{I}_{L,P}$ and $\bar{I}'_{L,S}$. The transferred power P is given in (1), where ϕ denotes the phase shift angle between $v_P(t)$ and $v'_S(t)$ and f_{sw} denotes the switching frequency [15].

$$P = \frac{V_P V'_S}{2\pi^2 f_{sw} L} \cdot \phi(\pi - |\phi|) \tag{1}$$

Maximum power is transferred for a phase shift angle of $\pi/2$. The turn-off transition in both H-Bridges is generally hard-switched, but for the turn-on transition, zero voltage switching (ZVS) is achieved for most operating points [16].

3 Analytical Model of SPS Modulation

In this section, an analytical model of the SPS modulation is presented, as FCM is directly derived from SPS modulation. The derived equations will be useful to compare the SPS and the FCM modulation strategies, e.g. in terms of losses. Section 3.1 provides an analysis of the current in the AC link which transfers power between the two DC ports. Section 3.2 gives an analysis of the magnetization of the transformer.

Because of the waveform symmetries as seen in Fig. 2, it is sufficient to regard half a switching period. The following conventions are made: For positive phase shifts $\phi \geq 0$, the rising edge of the primary voltage $v_P(t)$ is located at $\omega_{sw}t = 0$ and the rising edge of the secondary voltage $v'_S(t)$ is delayed to $\omega_{sw}t = \phi$. For negative phase shifts $\phi < 0$, the rising edge of the secondary voltage is located at $\omega_{sw}t = 0$ and the rising edge of the primary voltage is delayed to $\omega_{sw}t = |\phi|$. Those conventions are visualized in Fig. 3.

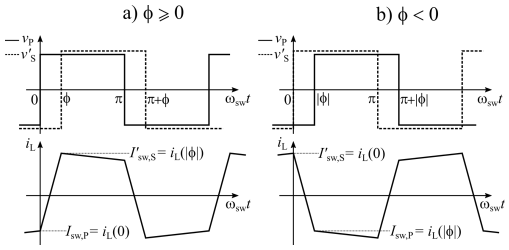

Figure 3: Timing conventions for the analytical models.

3.1 Line Current Waveform

The current waveform $i_L(\omega_{sw}t)$ is obtained by integrating the output voltage difference of the H-Bridges, $v_P(t) - v'_S(t)$, which drops on the leakage inductance L. For keeping the model simple, all ohmic resistances and the magnetizing inductance L_m are neglected in this analysis, as L_m is usually much bigger than the leakage inductance L. The resulting current waveform as well as its initial values for $\omega_{sw}t = 0$ and $\omega_{sw}t = |\phi|$ are given as follows:

$$i_L(\omega_{sw}t) = \begin{cases} i_L(0) + \mathrm{sgn}(\phi)\frac{V_P + V'_S}{\omega_{sw}L}\omega_{sw}t \\ \qquad\qquad \text{for } 0 \leq \omega_{sw}t < |\phi| \\ i_L(|\phi|) + \frac{V_P - V'_S}{\omega_{sw}L}(\omega_{sw}t - |\phi|) \\ \qquad\qquad \text{for } |\phi| \leq \omega_{sw}t < \pi \end{cases} \tag{2}$$

$$i_L(0) = -\frac{1}{2}\left(\frac{V_P + V'_S}{\omega_{sw}L}\phi + \frac{V_P - V'_S}{\omega_{sw}L}(\pi - |\phi|)\right) \tag{3}$$

$$i_L(|\phi|) = +\frac{1}{2}\left(\frac{V_P + V'_S}{\omega_{sw}L}\phi - \frac{V_P - V'_S}{\omega_{sw}L}(\pi - |\phi|)\right) \tag{4}$$

The peak value of the AC link current i_L is denoted $\hat{I}_L$:

$$\begin{aligned} \hat{I}_L &= \max\left[|i_L(0)|,\ |i_L(|\phi|)|\right] \\ &= \frac{|V_P - V'_S|}{2\omega_{sw}L}\pi + \frac{(V_P + V'_S) - |V_P - V'_S|}{2\omega_{sw}L}|\phi| \end{aligned} \tag{5}$$

By squaring (2) and integrating, the RMS value of the AC link current, I_L, is also derived:

$$I_\mathrm{L} = \frac{1}{\omega_\mathrm{sw} L}\sqrt{\frac{\pi^2}{12}(V_\mathrm{P} - V_\mathrm{S}^{'})^2 + V_\mathrm{P} V_\mathrm{S}^{'}\left(\phi^2 - \frac{8}{12\pi}|\phi|^3\right)} \tag{6}$$

The input currents of the two H-Bridges, $i_{\mathrm{L,P}}(t)$ and $i_{\mathrm{L,S}}^{'}(t)$, as shown in Fig. 2d and Fig. 2e, are obtained by changing the sign of i_L in a way such that it accounts for the switching state of the respective H-Bridges. If pure DC currents are assumed at the two ports of the DAB, the ripples of $i_{\mathrm{L,P}}(t)$ and $i_{\mathrm{L,S}}^{'}(t)$ flow into the DC capacitors C_P and C_S. The ripple charges ΔQ_P and $\Delta Q_\mathrm{S}^{'}$ are assessed by calculating the areas enclosed by the waveforms $\left(i_{\mathrm{L,P}}(\omega_\mathrm{sw} t) - \bar{I}_{\mathrm{L,P}}\right)$ and $\left(i_{\mathrm{L,S}}^{'}(\omega_\mathrm{sw} t) - \bar{I}_{\mathrm{L,S}}^{'}\right)$. The results are shown in equations (11) and (12).

3.2 Transformer Utilization in SPS Modulation

This section presents an in-depth analysis of the transformer utilization in SPS modulation. The transformer is modeled by its T-equivalent circuit, which is shown in Fig. 4. The inductances $L_{\mathrm{P}\sigma}$ and $L_{\mathrm{S}\sigma}^{'}$ describe the stray inductances of the transformer on both the primary and secondary windings, but shall include, if present, external series inductors, so that $L = L_{\mathrm{P}\sigma} + L_{\mathrm{S}\sigma}^{'}$.

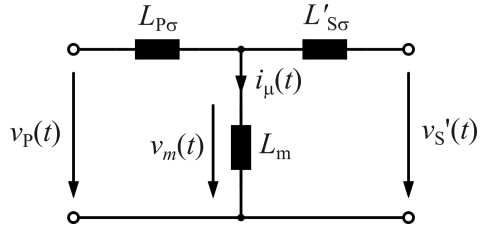

Figure 4: T-equivalent circuit of the transformer.

The quantities r, d and λ as given in (7)-(9) are defined as follows: r is the ratio of the stray inductances $L_{\mathrm{P}\sigma}$ over $L_{\mathrm{S}\sigma}^{'}$ and ranges from 0 to ∞. d is the ratio of the voltages V_P over $V_\mathrm{S}^{'}$ and describes how well the transformer turns ratio n matches the actual ratio of the DC voltages. λ is a new quantity called *transformer utilization factor*. Its maximum value of 1 is reached for $r = d$, and it decays to zero if there is no inductance present on either side of the transformer ($r = 0$ or $r \to \infty$):

$$r = \frac{L_{\mathrm{P}\sigma}}{L_{\mathrm{S}\sigma}^{'}} \tag{7}$$

$$d = \frac{V_\mathrm{P}}{V_\mathrm{S}^{'}} = \frac{V_\mathrm{P}}{n V_\mathrm{S}} \tag{8}$$

$$\lambda = 1 - \frac{|V_\mathrm{P} - r V_\mathrm{S}^{'}|}{V_\mathrm{P} + r V_\mathrm{S}^{'}} = 1 - \frac{|d - r|}{d + r} \tag{9}$$

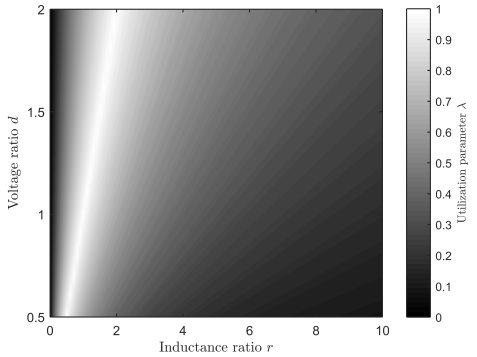

Figure 5: Transformer utilization parameter λ as function of leakage inductance ratio r and voltage ratio d.

Using definitions (7)-(9) and the assumption that the stray inductances are much smaller than L_m (but not necessarily equal), the virtual voltage v_m on the magnetizing inductance can be calculated from nodal analysis of the circuit in Fig. 4:

$$v_\mathrm{m}(t) = \frac{v_\mathrm{P}(t) + r v_\mathrm{S}^{'}(t)}{1 + r} = \begin{cases} v_\mathrm{P}(t) & \text{for } r = 0 \\ \frac{v_\mathrm{P}(t) + v_\mathrm{S}^{'}(t)}{2} & \text{for } r = 1 \\ v_\mathrm{S}^{'}(t) & \text{for } r \to \infty \end{cases} \tag{10}$$

$$\Delta Q_\mathrm{P} = \begin{cases} \frac{(2V_\mathrm{S}^{'}\phi^2 + \pi^2(V_\mathrm{P} - V_\mathrm{S}^{'}))^2}{8\omega_\mathrm{sw}^2 L \pi^2 (V_\mathrm{P} - V_\mathrm{S}^{'})} & \text{for } V_\mathrm{P} > V_\mathrm{S}^{'} \text{ and } |I_{\mathrm{sw,S}}^{'}| < |\bar{I}_{\mathrm{L,P}}| \\ \frac{(2V_\mathrm{S}^{'}|\phi|(2\pi - |\phi|) + \pi^2(V_\mathrm{P} - V_\mathrm{S}^{'}))^2}{8\omega_\mathrm{sw}^2 L \pi^2 (V_\mathrm{P} + V_\mathrm{S}^{'})} & \text{for } \begin{cases} V_\mathrm{P} = V_\mathrm{S}^{'} \text{ or} \\ V_\mathrm{P} > V_\mathrm{S}^{'} \text{ and } |I_{\mathrm{sw,S}}^{'}| \geq |\bar{I}_{\mathrm{L,P}}| \text{ or} \\ V_\mathrm{P} < V_\mathrm{S}^{'} \text{ and } |I_{\mathrm{sw,P}}| \geq |\bar{I}_{\mathrm{L,P}}| \end{cases} \\ \frac{V_\mathrm{S}^{'}(2V_\mathrm{S}^{'}\phi^2 - (\pi^2 - 2\pi|\phi|)(V_\mathrm{P} - V_\mathrm{S}^{'}))^2}{4\omega_\mathrm{sw}^2 L \pi^2 (V_\mathrm{S}^{'2} - V_\mathrm{P}^2)} & \text{for } V_\mathrm{P} < V_\mathrm{S}^{'} \text{ and } |I_{\mathrm{sw,P}}| < |\bar{I}_{\mathrm{L,P}}| \end{cases} \tag{11}$$

$$\Delta Q_\mathrm{S}^{'} = \begin{cases} \frac{V_\mathrm{P}(2V_\mathrm{P}\phi^2 + (\pi^2 - 2\pi|\phi|)(V_\mathrm{P} - V_\mathrm{S}^{'}))^2}{4\omega_\mathrm{sw}^2 L \pi^2 (V_\mathrm{P}^2 - V_\mathrm{S}^{'2})} & \text{for } V_\mathrm{P} > V_\mathrm{S}^{'} \text{ and } |I_{\mathrm{sw,S}}^{'}| < |\bar{I}_{\mathrm{L,S}}^{'}| \\ \frac{(2V_\mathrm{P}|\phi|(2\pi - |\phi|) - \pi^2(V_\mathrm{P} - V_\mathrm{S}^{'}))^2}{8\omega_\mathrm{sw}^2 L \pi^2 (V_\mathrm{P} + V_\mathrm{S}^{'})} & \text{for } \begin{cases} V_\mathrm{P} = V_\mathrm{S}^{'} \text{ or} \\ V_\mathrm{P} > V_\mathrm{S}^{'} \text{ and } |I_{\mathrm{sw,S}}^{'}| \geq |\bar{I}_{\mathrm{L,S}}^{'}| \text{ or} \\ V_\mathrm{P} < V_\mathrm{S}^{'} \text{ and } |I_{\mathrm{sw,P}}| \geq |\bar{I}_{\mathrm{L,S}}^{'}| \end{cases} \\ \frac{(2V_\mathrm{P}\phi^2 - \pi^2(V_\mathrm{P} - V_\mathrm{S}^{'}))^2}{8\omega_\mathrm{sw}^2 L \pi^2 (V_\mathrm{S}^{'} - V_\mathrm{P})} & \text{for } V_\mathrm{P} < V_\mathrm{S}^{'} \text{ and } |I_{\mathrm{sw,P}}| < |\bar{I}_{\mathrm{L,S}}^{'}| \end{cases} \tag{12}$$

Using the SPS switching pattern and integrating this equation gives the magnetizing current waveform $i_\mu(\omega_{sw}t)$:

$$i_\mu(\omega_{sw}t) = \begin{cases} i_\mu(0) + \mathrm{sgn}(\phi)\frac{V_P - rV_S'}{(1+r)\omega_{sw}L_m}\omega_{sw}t \\ \qquad \text{for } 0 \le \omega_{sw}t < |\phi| \\ i_\mu(|\phi|) + \frac{V_P + rV_S'}{(1+r)\omega_{sw}L_m}(\omega_{sw}t - |\phi|) \\ \qquad \text{for } |\phi| \le \omega_{sw}t < \pi \end{cases} \quad (13)$$

$$i_\mu(0) = -\frac{1}{2}\left(\frac{V_P - rV_S'}{(1+r)\omega_{sw}L_m}\phi + \frac{V_P + rV_S'}{(1+r)\omega_{sw}L_m}(\pi - |\phi|)\right) \quad (14)$$

$$i_\mu(|\phi|) = +\frac{1}{2}\left(\frac{V_P - rV_S'}{(1+r)\omega_{sw}L_m}\phi - \frac{V_P + rV_S'}{(1+r)\omega_{sw}L_m}(\pi - |\phi|)\right) \quad (15)$$

The flux linkage in the transformer core equals $\psi = L_m i_\mu$, as shown in Fig. 2b. In analogy to (5), the peak magnetizing current $\hat{I}_\mu$ and the peak flux linkage $\hat{\psi}$ are calculated:

$$\begin{aligned}\hat{I}_\mu &= \max\left[|i_\mu(0)|,\ |i_\mu(|\phi|)|\right] \\ &= \frac{V_P + rV_S'}{2(1+r)\omega_{sw}L_m}\pi - \frac{(V_P + rV_S') - |V_P - rV_S'|}{2(1+r)\omega_{sw}L_m}|\phi| \end{aligned} \quad (16)$$

$$\hat{\psi} = \frac{V_P + rV_S'}{2(1+r)\omega_{sw}}\pi - \frac{(V_P + rV_S') - |V_P - rV_S'|}{2(1+r)\omega_{sw}}|\phi| \quad (17)$$

From (17), it becomes clear that the maximum peak flux linkage in the transformer core, $\hat{\psi}_{max}$, is reached for $\phi = 0$:

$$\hat{\psi}_{max} = \frac{V_P + rV_S'}{2(1+r)\omega_{sw}}\pi \quad (18)$$

The flux density B cannot be calculated as the number of turns and the core area are unknown. However, if a reasonable value is assumed for the maximum flux density, e.g. $\hat{B}_{max} = 200\,\mathrm{mT}$ for a ferrite core, the per-unit utilization of the transformer can be derived as given by (19), based on the utilization factor λ from (9).

$$\frac{\hat{B}}{\hat{B}_{max}} = \frac{\hat{\psi}}{\hat{\psi}_{max}} = 1 - \lambda\frac{|\phi|}{\pi} \quad (19)$$

The second term in (19) is always positive which means that the flux linkage is decreasing with increasing phase shift. Therefore, the transformer is utilized at its maximum for zero phase shift, i.e. zero power transfer. Hence, the transformer *has to be designed for no load*. This is the main finding of the analysis of the DAB which will be addressed by FCM in section 4.

The iron losses of the transformer are calculated using the improved generalized STEINMETZ equation (iGSE):

$$P_{Fe} = Vol_{Fe} f_{sw} \int_0^{f_{sw}^{-1}} k_i \left|\frac{\mathrm{d}B}{\mathrm{d}t}\right|^\alpha \Delta\hat{B}_{pp}^{\beta-\alpha}\mathrm{d}t, \text{ where} \quad (20)$$

$$k_i = \frac{k}{(2\pi)^{\alpha-1}\int_0^{2\pi}|\cos\theta|^\alpha \cdot 2^{\beta-\alpha}\mathrm{d}\theta} \quad (21)$$

k, α and β are material specific data, Vol_{Fe} is the iron volume and $\Delta\hat{B}_{pp}$ is the peak-to-peak core flux density. The cross-sectional area of the core and the number of turns are not always known. Therefore, the per-unit quantity $\hat{B}/\hat{B}_{max}$ from (19) has to be used in (20), which now can be solved analytically:

$$P_{Fe} = 2^{\alpha+\beta} Vol_{Fe} k_i f_{sw}^\alpha \hat{B}_{max}^\beta \left(1 - \lambda\frac{|\phi|}{\pi}\right)^{\beta-\alpha}\left(1 - \lambda_\alpha\frac{|\phi|}{\pi}\right) \quad (22)$$

$$\text{where } \lambda_\alpha = 1 - \left(\frac{|d-r|}{d+r}\right)^\alpha$$

The only unknown quantity is the volume of the transformer core and it is assessed by the stored energy E_m. This energy is expressed by the peak flux linkage and the magnetizing current on the one hand and by the peak flux density on the other hand:

$$\begin{aligned} E_m = \frac{1}{2}L_m\hat{I}_\mu^2 = \frac{1}{2}\hat{\psi}_{max}\hat{I}_\mu = Vol_{Fe}\cdot\frac{\hat{B}_{max}^2}{2\mu_0\mu_r} \\ \Rightarrow\ Vol_{Fe} = \frac{\mu_0\mu_r\hat{\psi}_{max}\hat{I}_\mu}{\hat{B}_{max}^2} \end{aligned} \quad (23)$$

4 Flux Control Modulation

Equation (19) shows that the transformer flux linkage decreases with phase shift as long as there is some inductance on both sides of the transformer ($\lambda \neq 0$). As already stated, this implies that the transformer is actually designed for no load. The idea of FCM is to reduce the switching frequency linearly as the phase shift increases, to counteract the linear reduction in transformer utilization as shown in (19). The highest switching frequency, $f_{sw,max}$, is used at no load, i.e. $\phi = 0$. Equations (18) and (19) are thus modified as follows:

$$\hat{\psi}_{max} = \frac{V_P + rV_S'}{2(1+r)\omega_{sw,max}}\pi \quad (24)$$

$$\frac{\hat{B}}{\hat{B}_{max}} = \frac{\hat{\psi}}{\hat{\psi}_{max}} = \frac{f_{sw,max}}{f_{sw}}\cdot\left(1 - \lambda\frac{|\phi|}{\pi}\right) \quad (25)$$

The transformer utilization is kept constant by setting (25) to unity and solving for the switching frequency. Using this result in the power equation (1) gives a new modulation technique, called Flux Control Modulation (FCM), defined by (26) and (27):

$$f_{sw} = f_{sw,max}\left(1 - \lambda\frac{|\phi|}{\pi}\right) \quad (26)$$

$$P = \frac{V_P V_S'}{2\pi f_{sw,max}L}\cdot\phi\frac{\pi - |\phi|}{\pi - \lambda|\phi|} \quad (27)$$

The power equation (27) is depicted in Fig. 6 for different utilization parameters λ between 0 and 1. As the utilization parameter λ approaches unity, the power equation (27) converges into a linear function, which is convenient for control:

$$P \approx \frac{V_P V_S'}{2\pi f_{sw,max}L}\cdot\phi \quad \text{for} \quad \lambda \approx 1 \quad (28)$$

Because of the linear decay in switching frequency (26), switching losses are reduced with increasing power. Another big advantage is the linearization of the power characteristic and its

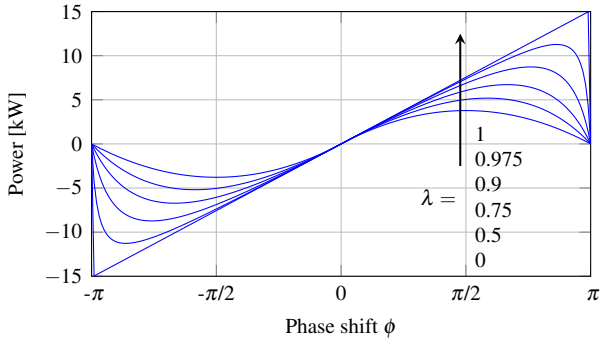

Figure 6: Power transfer for FCM modulation as a function of phase shift and $\lambda = 0, 0.5, 0.75, 0.9, 0.975, 1$. The linear function corresponds to $\lambda = 1$. $V_P = 270\,\text{V}$, $V_S = 28\,\text{V}$, $n = 10$, $f_{sw,max} = 100\,\text{kHz}$, $L = 25\,\mu\text{H}$.

ease of implementation on a control platform. One disadvantage of FCM are increased iron losses, although the iron losses might not play a dominant role in the overall loss balance of the converter. Additionally, FCM covers a broader range of switching frequencies, which may be more demanding for EMI filtering.

The iron losses under FCM are assessed by solving the iGSE (20) and substituting the switching frequency f_{sw} by the expression in (26):

$$P_{Fe,FCM} = 2^{\alpha+\beta} Vol_{Fe} k_i f_{sw,max}^{\alpha} \hat{B}_{max}^{\beta} \cdot \left(1 - \lambda_{\alpha} \frac{|\phi|}{\pi}\right) \tag{29}$$

5 Comparison Between SPS and FCM

The SPS modulation is identified as the special case of FCM when $\lambda = 0$, as in this case (27) degenerates into (1) and (26) implies $f_{sw} = f_{sw,max}$. A utilization factor of $\lambda = 0$ is particularly the case if there is no inductance on one side of the transformer ($r = 0$ or $r \to \infty$). In any other case, FCM is advantageous to use, especially in the case of $\lambda = 1$, yielding the maximum reduction in switching losses.

The duality between SPS modulation and FCM is presented in the following: In SPS modulation, the frequency is kept at its maximum value and the transformer flux linkage decays with increasing phase shift. However, in FCM, the flux linkage is kept at its maximum value and the switching frequency is reduced. The roles of switching frequency and flux linkage are swapped, as visualized in Fig. 7.

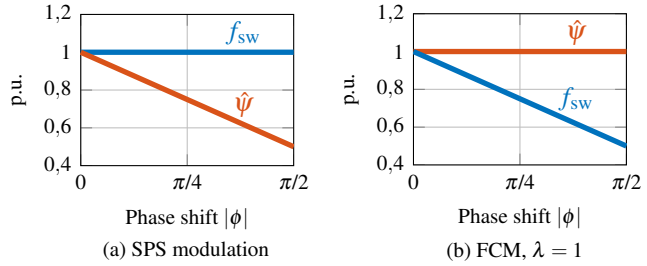

Figure 7: Normalized frequency and flux linkage comparison for SPS modulation and FCM.

From Fig. 6, it becomes clear that in FCM a smaller phase shift is needed compared to SPS modulation. The required phase shift angles for SPS modulation and FCM are plotted in Fig. 8a. For SPS modulation, the required phase shift angle ϕ_{SPS} is obtained as a complex equation (30) by solving (1), while the phase shift angle ϕ_{FCM} in FCM is given by a simpler equation (31).

$$\phi_{SPS} = \text{sgn}(P) \left(\frac{\pi}{2} - \sqrt{\frac{\pi^2}{4} - \frac{2\pi^2 f_{sw,max} L}{V_P V_S'} \cdot |P|} \right) \tag{30}$$

$$\phi_{FCM} \approx \frac{2\pi f_{sw,max} L}{V_P V_S'} \cdot P \quad \text{for} \quad \lambda \approx 1 \tag{31}$$

Because of the frequency reduction in FCM, the switching losses P_{sw} are reduced compared to SPS modulation as given in (32). In contrast, the iron losses P_{Fe} are increased as shown in (33), as the transformer is fully utilized in FCM.

$$P_{sw,FCM} = P_{sw,SPS} \cdot \left(1 - \lambda \frac{|\phi|}{\pi}\right) \leq P_{sw,SPS} \tag{32}$$

$$P_{Fe,FCM} = \frac{P_{Fe,SPS}}{\left(1 - \lambda \frac{|\phi|}{\pi}\right)^{\beta-\alpha}} \geq P_{Fe,SPS} \tag{33}$$

Some further comparisons between SPS modulation and FCM can be made: If the frequency equation of FCM (26) is substituted into (5), the peak current in the AC link under FCM is obtained. It is plotted, normalized to SPS modulation, in Fig. 8b. Similarly, substituting (26) into (6), the RMS current in the AC link under FCM is plotted in Fig. 8c. Finally, Fig. 8d shows the primary side ripple charge from (11) in FCM compared to SPS modulation. It is observed that neither peak nor RMS current in the AC link increase as a consequence of FCM. This implies that also the conduction losses are reduced in FCM. It could be assumed that the ripple charges would increase as a consequence of frequency reduction, but it is found that this is not the case. The reason for all those effects is that even though the frequency is reduced in FCM, a smaller phase shift than in SPS modulation is needed, as it is shown in Fig. 8a.

6 Performance Validation

The effectiveness of FCM has been validated by a PLECS simulation of the DAB of the ASPIRE project. The system parameters used are given in Table 1.

Table 1: PLECS simulation parameters.

DC voltages	V_P, V_S	270 V, 28 V
Rated power	P	3 kW
Max. switching frequency	$f_{sw,max}$	100 kHz
Transformer turns ratio	n	10
Total leakage inductance	L	25 µH
Leakage inductance ratio	r	1
Magnetizing inductance	L_m	1 mH
Magnetic material	Ferroxcube	3C96
Maximum flux density	B_{max}	150 mT
Primary side MOSFET	Rohm	SCT3017AL (SiC)
Secondary side MOSFET	Infineon	2x IRF7759L2 (Si)

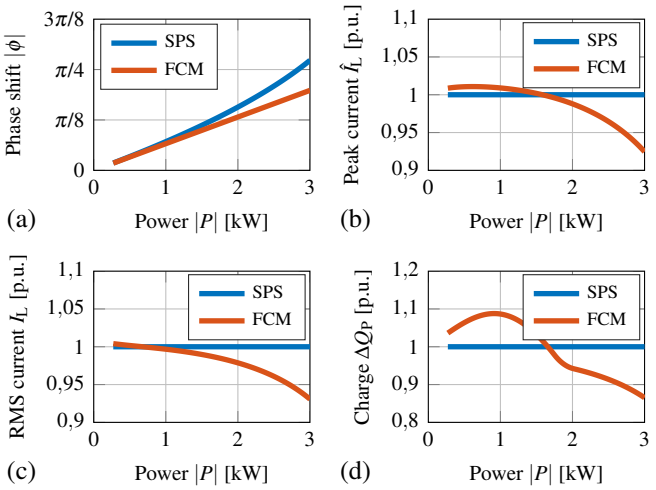

Figure 8: Comparison between SPS modulation and FCM. (a) Required phase shift angles for both modulation techniques. (b) Peak AC link current. (c) RMS AC link current. (d) Primary ripple charge. Plots (b)-(d) are normalized to SPS modulation. $V_P = 270\,\text{V}$, $V_S = 28\,\text{V}$, $n = 10$, $f_{sw,max} = 100\,\text{kHz}$, $L = 25\,\mu\text{H}$.

Fig. 9 shows the efficiency of the DAB, plotted against transferred power, when the same converter is operated with SPS and FCM modulation techniques. The reduction of switching losses in FCM yields an efficiency improvement of 0.46 % at full load.

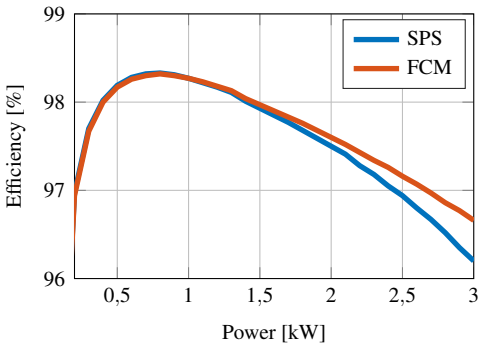

Figure 9: Efficiency of the DAB when operated with SPS modulation and FCM.

Finally, in Fig. 10, the transformer flux linkage $\psi(t)$ is plotted during a step load change from 500 W to 3 kW for both modulation strategies. It is clearly visible that in SPS modulation, the peak flux linkage decreases with increasing power. In FCM, however, the magnitude of the flux linkage is kept constant.

7 Conclusion

Flux Control Modulation is proposed in this paper and offers many advantages, such as reduced converter losses, improved transformer utilization and simplification of control design. It linearizes the power transfer characteristic of the DAB and hence making it suitable for analog control. The advantages of the proposed modulation technique have been validated by simulation.

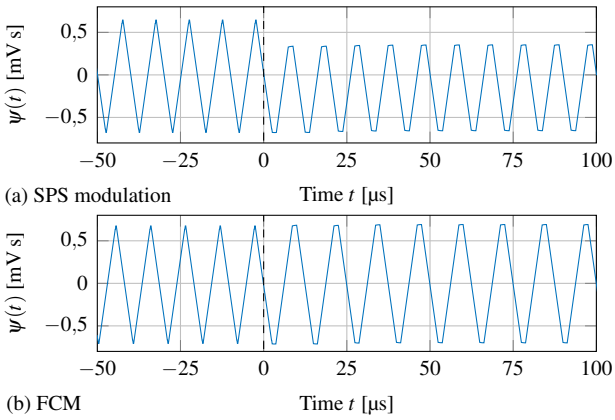

Figure 10: Flux linkage in the transformer core during a step load change from 500 W to 3 kW ($t = 0$) for SPS modulation and FCM.

Acknowledgment

This project has received funding from the Clean Sky 2 Joint Undertaking under the European Union's Horizon 2020 research and innovation programme under grant agreement No 717091.

References

[1] P. Wheeler and S. Bozhko. 'The More Electric Aircraft: Technology and challenges'. In: *IEEE Electrification Magazine* 2.4 (2014), pp. 6–12.

[2] P. Wheeler. 'Technology for the more and all electric aircraft of the future'. In: *2016 IEEE International Conference on Automatica (ICA-ACCA)*. 2016.

[3] H. Bai and C. Mi. 'Eliminate Reactive Power and Increase System Efficiency of Isolated Bidirectional Dual-Active-Bridge DC–DC Converters Using Novel Dual-Phase-Shift Control'. In: *IEEE Transactions on Power Electronics* 23.6 (2008), pp. 2905–2914.

[4] G. G. Oggier et al. 'Switching Control Strategy to Minimize Dual Active Bridge Converter Losses'. In: *IEEE Transactions on Power Electronics* 24.7 (2009), pp. 1826–1838.

[5] H. van Hoek et al. 'Enhanced Modulation Strategy for a Three-Phase Dual Active Bridge - Boosting Efficiency of an Electric Vehicle Converter'. In: *IEEE Transactions on Power Electronics* 28.12 (Dec. 2013), pp. 5499–5507.

[6] F. Krismer et al. 'Performance Optimization of a High Current Dual Active Bridge with a Wide Operating Voltage Range'. In: *IEEE Power Electronics Specialists Conference (PESC)*. IEEE, 2006.

[7] F. Krismer and J. W. Kolar. 'Closed Form Solution for Minimum Conduction Loss Modulation of DAB Converters'. In: *IEEE Transactions on Power Electronics* 27.1 (2012), pp. 174–188.

[8] F. Krismer and J. W. Kolar. 'Efficiency-Optimized High-Current Dual Active Bridge Converter for Automotive Applications'. In: *IEEE Transactions on Industrial Electronics* 59.7 (2012), pp. 2745–2760.

[9] R. Piveta et al. 'Circulating current mitigation in Dual Active Bridge converter'. In: *2015 IEEE 13th Brazilian Power Electronics Conference and 1st Southern Power Electronics Conference (COBEP/SPEC)*. Nov. 2015.

[10] H. van Hoek et al. 'Enhanced operating strategy for a three-phase dual-active-bridge converter including frequency variation'. In: *2015 IEEE 11th International Conference on Power Electronics and Drive Systems*. June 2015, pp. 492–498.

[11] A. Rodriguez et al. 'Different Purpose Design Strategies and Techniques to Improve the Performance of a Dual Active Bridge With Phase-Shift Control'. In: *IEEE Transactions on Power Electronics* 30.2 (2015), pp. 790–804.

[12] J. Everts et al. 'Optimal ZVS Modulation of Single-Phase Single-Stage Bidirectional DAB AC–DC Converters'. In: *IEEE Transactions on Power Electronics* 29.8 (2014), pp. 3954–3970.

[13] F. Jauch and J. Biela. 'Generalized modeling and optimization of a bidirectional dual active bridge DC-DC converter including frequency variation'. In: *International Power Electronics Conference (IPEC - ECCE ASIA)*. IEEE, 2014.

[14] J. Hiltunen et al. 'Variable-Frequency Phase Shift Modulation of a Dual Active Bridge Converter'. In: *IEEE Transactions on Power Electronics* 30.12 (2015), pp. 7138–7148.

[15] R. W. De Doncker et al. 'A Three-phase Soft-Switched High-Power-Density dc /dc Converter for High-Power Applications'. In: *IEEE Transactions on Industry Applications* 27.1 (1991), pp. 63–73.

[16] S. Taraborrelli et al. 'Bidirectional dual active bridge converter using a tap changer for extended voltage ranges'. In: *2016 18th European Conference on Power Electronics and Applications (EPE '16 ECCE Europe)*. Institute of Electrical and Electronics Engineers (IEEE), Sept. 2016.